applied sciences

MDPI

Article

Analysis of the Load-Bearing Capacity of Pebble Aggregates

Pan Liu *, Peiyi Bai and Wenju Liu

College of Vehicle and Traffic Engineering, Henan University of Science and Technology, Luoyang 471003, China; baipeiyi2023@163.com (P.B.); liuwenju@stu.haust.edu.cn (W.L.)
* Correspondence: liupan@haust.edu.cn

Abstract: The load-bearing capacity of pebble aggregates plays a pivotal role in influencing the operational performance of uncontrolled trucks on arrester beds. The complexity of this phenomenon stems from the nonuniformity in the shapes of the pebbles and their stochastic arrangement within the beds, presenting notable challenges for traditional mathematical modelling techniques in precisely evaluating the contact dynamics of these aggregates. This study leverages the discrete element method (DEM) to extensively analyse the arrester bed aggregate of a standard truck escape ramp. The aforementioned mechanism entails the gathering of morphological parameters of irregularly shaped aggregate particles and introduces a novel method for constructing random shapes that adhere to the observed distribution characteristics. A discrete element model, grounded in the physical properties of these aggregates, is formulated. This study focuses on the aggregate's load-bearing capabilities, scrutinising the mechanical behaviour of the aggregate particles at the macroscopic and microscopic scales. These insights offer substantial scientific contributions and practical implications for assessing the safety of escape ramps and determining essential parameters for the brake bed design.

Keywords: pebble aggregates; load-bearing capacity; truck escape ramp; arrester beds; discrete element method (DEM)

check for updates

Citation: Liu, P.; Bai, P.; Liu, W. Analysis of the Load-Bearing Capacity of Pebble Aggregates. *Appl. Sci.* **2024**, *14*, 3109. https://doi.org/10.3390/app14073109

Academic Editors: Iran Rocha Segundo and Joaquim Carneiro

Received: 6 March 2024
Revised: 31 March 2024
Accepted: 4 April 2024
Published: 8 April 2024

Copyright: © 2024 by the authors. Licensee MDPI, Basel, Switzerland. This article is an open access article distributed under the terms and conditions of the Creative Commons Attribution (CC BY) license (https://creativecommons.org/licenses/by/4.0/).

1. Introduction

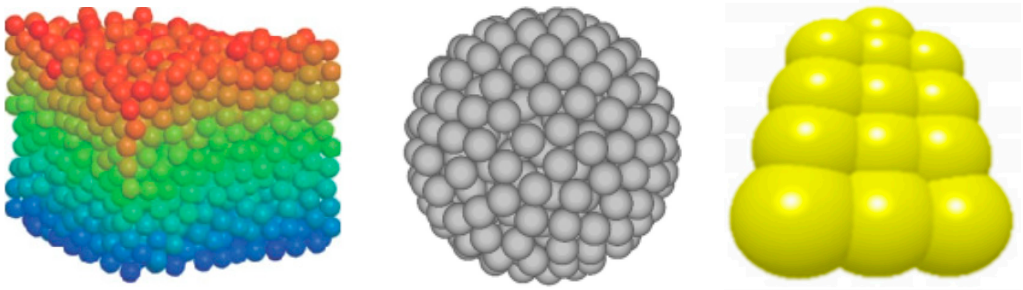
Brake failure in heavy trucks significantly contributes to severe traffic accidents [1]. A type of auxiliary lane, referred to as a truck escape ramp (TER), has been developed to mitigate these accidents. Figure 1 illustrates the fundamental design of the TER, which aims to decelerate trucks through the rolling resistance induced between the truck tires and the arrester beds, typically composed of pebble aggregates. Since the construction of the first TER in California, research on TERs has mainly focused on predicting brake drum temperatures [2], determining truck departure angles [3], exploring alternative materials for arrester bed pavements [4] and other related aspects. However, a significant knowledge gap exists regarding the load-bearing capacity of irregularly shaped, randomly distributed pebble aggregates in arrester beds, which directly influences the safety performance of trucks navigating through these beds.



Figure 1. Truck escape ramp.

Advancements in computational technology have significantly enhanced the recognition of the discrete element method (DEM) as an exceptionally effective approach for investigating interaction mechanisms within pebble aggregates [5]. The DEM leverages Newtonian mechanics to analyse the contact forces amongst these elements by representing particles as discrete entities, offering a detailed perspective at the particle level. This method utilises time steps to accurately compute the resultant forces and motions of particles, thus facilitating an extensive understanding of their dynamics. The DEM, originally developed by Cundall to address rock mechanics [6], has been extensively applied across various fields. The DEM application spans from analysing road materials in highway engineering [7,8], to investigating soil interaction mechanics [9–11], to constructing simplified models for trucks on roads with discrete pebble surfaces [12,13]. This diverse application spectrum not only demonstrates the DEM's versatility but also significantly underscores its efficacy in assessing the load-bearing capacities of pebble aggregates.

The DEM provides a framework for the construction of particle shapes through three principal methodologies. The fundamental element construction method (Figure 2a) [14] converts basic geometric shapes, predominantly spheres, into diverse forms, such as triangles, cylinders and ellipsoids. This method enhances computational efficiency by lowering the computational requirements. Nonetheless, the application of the DEM is typically confined to regularly shaped pebbles, necessitating precise adjustments to the software's contact parameters for accommodating the varied geometries of different pebbles. The tangent element construction method (Figure 2b) [15] facilitates the modelling of intricate particle shapes with a precision that is dependent on the quantity of the basic elements utilized. This dependency significantly influences the computational load required for the modelling process. The overlapping element construction method (Figure 2c) [16] constructs the desired object by stacking basic elements. This approach skillfully balances computational efficiency with modelling precision. However, this approach demands careful consideration of the algorithm for computing the coordinates of these basic elements.



(**a**) (**b**) (**c**)

Figure 2. Particle shape construction method used in DEM. (**a**) fundamental element; (**b**) tangent element; (**c**) overlapping element.

Experimental methodologies play a crucial role in validating numerical simulations, especially in the domain of DEM simulations [17]. These methods are essential for calibrating and verifying the accuracy of DEM simulations, ensuring the reliability of their outcomes. The triaxial compression test [18,19] provides a detailed assessment of the pebble properties and their interaction dynamics. However, the effectiveness of this test in measuring the load-bearing capacity of pebble beds is limited due to the potential interference from the boundary walls. The shear test method [20,21] effectively examines the influence of pebble attributes on contact mechanisms. Nevertheless, the focus of this test on lateral compression, limits its application in evaluating the load-bearing characteristics of pebble beds. The hopper discharge analysis, detailed in references [22,23] and prevalent in sectors such as agriculture and medicine, excels in assessing how particle shape variations affect pebble properties. Nevertheless, the effectiveness of this method in analysing the load-compaction behaviour of pebble beds is limited. The open-top box compression test [12]

effectively mitigates wall effects common in close-packing tests and accurately assesses the load-bearing capacity of pebble beds, thus providing a comprehensive evaluation.

2. Numerical Simulations of the Randomly Shaped Pebbles

2.1. DEM-Based Shape Reconstruction Method for Irregularly Shaped Pebbles

The geometric shape of pebbles plays a pivotal role in determining the load-bearing capacity of arrester beds on truck escape ramps. This study is dedicated to examining the aggregates used in such beds and proposes a methodology for developing DEM models with Particle Flow Code Version 5.0 software. These models are capable of accurately simulating the complex three-dimensional and irregular shapes of pebble particles.

2.1.1. Materials

In this study, the tested pebbles were collected from a TER located at K209+400 Road, Gansu Province, China (Figure 3).

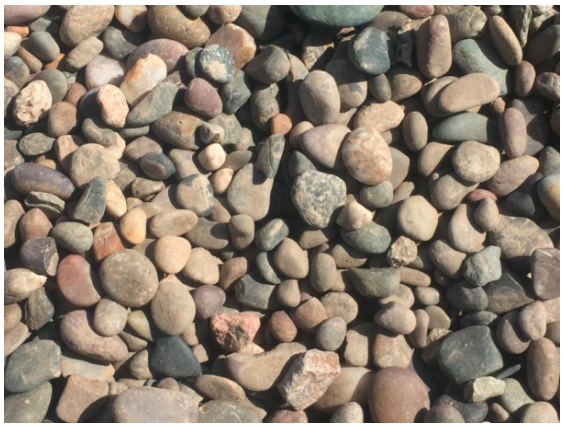


Figure 3. Tested pebbles.

One hundred pebbles were selected via a random sampling process [12]. Figure 4 presents the distribution of the pebble dimensions, including length, width and height.

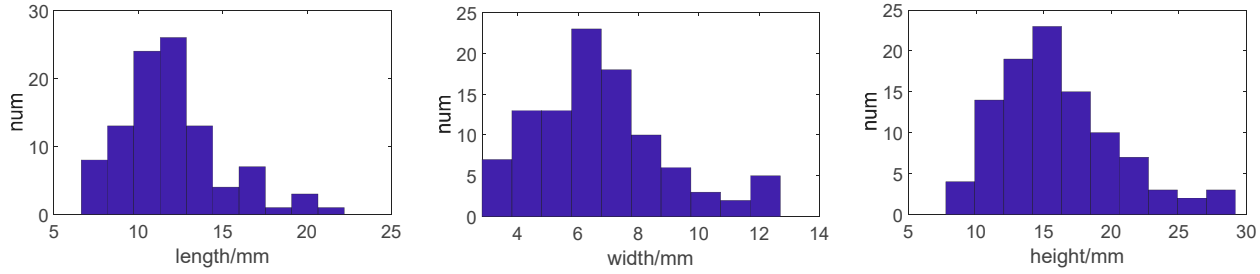


Figure 4. Distribution of the pebble dimensions (**a**) length; (**b**) width; (**c**) height.

2.1.2. Shape Reconstruction Method for the Irregularly Shaped Pebbles

Figure 5 depicts the method used to construct the shape of a single pebble, utilising it as an illustrative example.

Step 1: A single pebble was randomly selected, and its three views were precisely captured. The Canny edge detection algorithm [24] was employed to define the outlines of these views, which were then segmented into upper and lower parts. The outcomes demonstrate that this approach effectively captured the exterior shape of the selected pebble. A high-order polynomial fitting (Equation (1)) was then applied to each segment. The length of each view was standardised to 100 units before fitting, to facilitate calculation.

$$z = \sum_{i=1}^{7} a_i \cdot x \cdot (x - 100)^i \tag{1}$$

Step 2: The main and left views were filled with circular elements, with the parameters for each circle derived from Equations (2)–(4).

$$x_i = 100/n \cdot i(\mathrm{i} = 1, 2, 3 \ldots \mathrm{n}) \tag{2}$$

$$y_i = (z_u + z_l)/2 \tag{3}$$

$$r_i = (z_u - z_l)/2 \tag{4}$$

Step 3: A preliminary 3D model was constructed using the information derived from the circular elements observed in the left view. In this model, the position coordinates (x, y, z) of each spherical element were defined as 0, x_left and y_left, where x_left and y_left represent the horizontal and vertical coordinates of the circular elements in the left view, respectively. The radius of each spherical element matched the radius observed in the left view. The 3D model was then replicated and scaled multiple times based on the x-coordinates of the elements in the primary view. The x-coordinates of all elements were methodically adjusted throughout this scaling process to align with the x-coordinates of the circular elements in the primary view. The radii of the ball elements were recalculated based on the outline of the main view. This procedure was repeated for the ball elements based on the outline of the upper view.

Step 4: In light of the computational demands, simplified pebble DEM models were developed by reducing the number of spherical elements. Simulations of several pebbles were conducted to further substantiate the model's construction approach, with the outcomes illustrated in Figure 6. These findings indicate that the methodology effectively captures the pebble's shape.

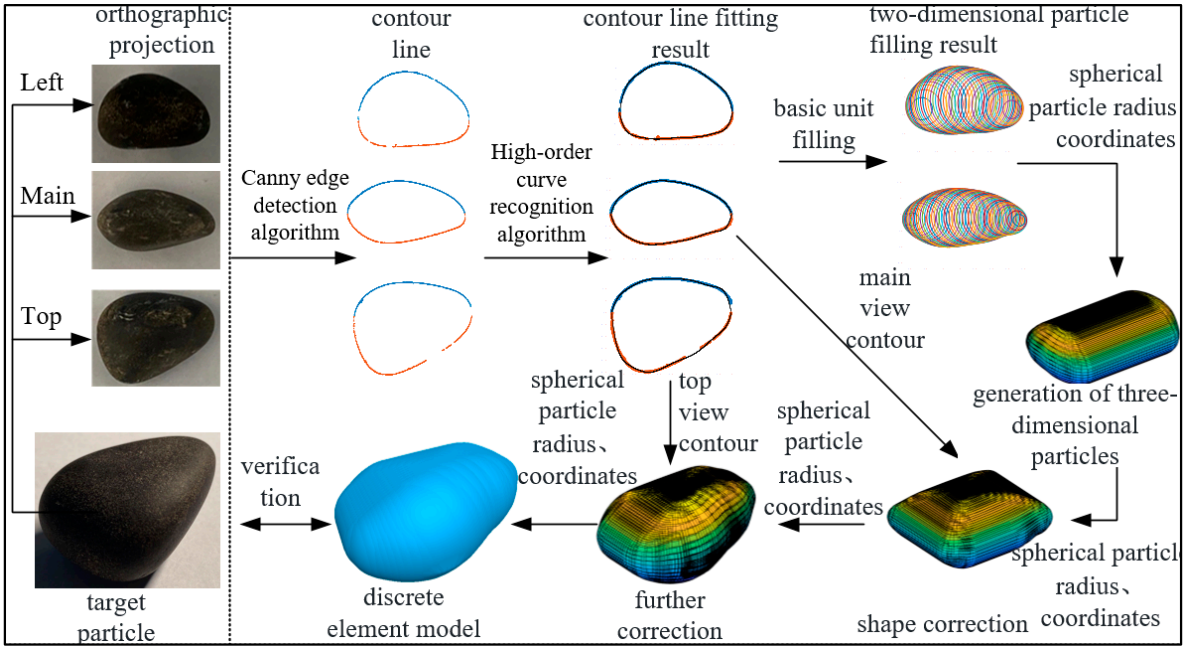


Figure 5. Methodology for constructing the shape of the pebble, DEM model.

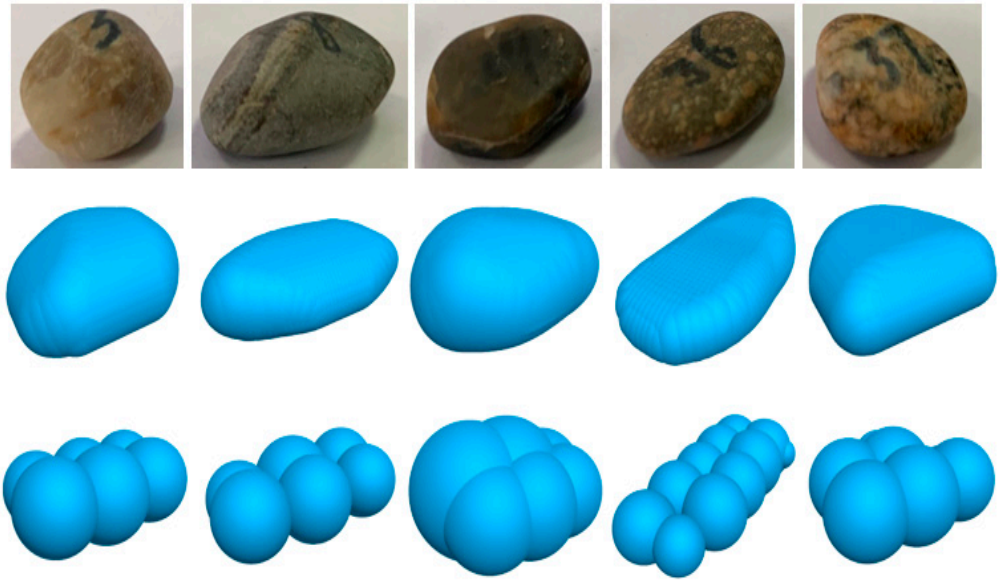


Figure 6. Developed pebble DEM models.

2.2. Pebble DEM Model Parameter Calibration and Model Validation

Considering the predominantly rigid nature of the pebbles, this study adopts the 'Linear Model' [24] as the fundamental DEM contact model for analysing pebble interactions. The key parameters of the pebble DEM model, particularly the friction parameter, are determined through open-top box compression tests, as detailed in [25]. The testing and simulation procedures are illustrated in Figure 7.

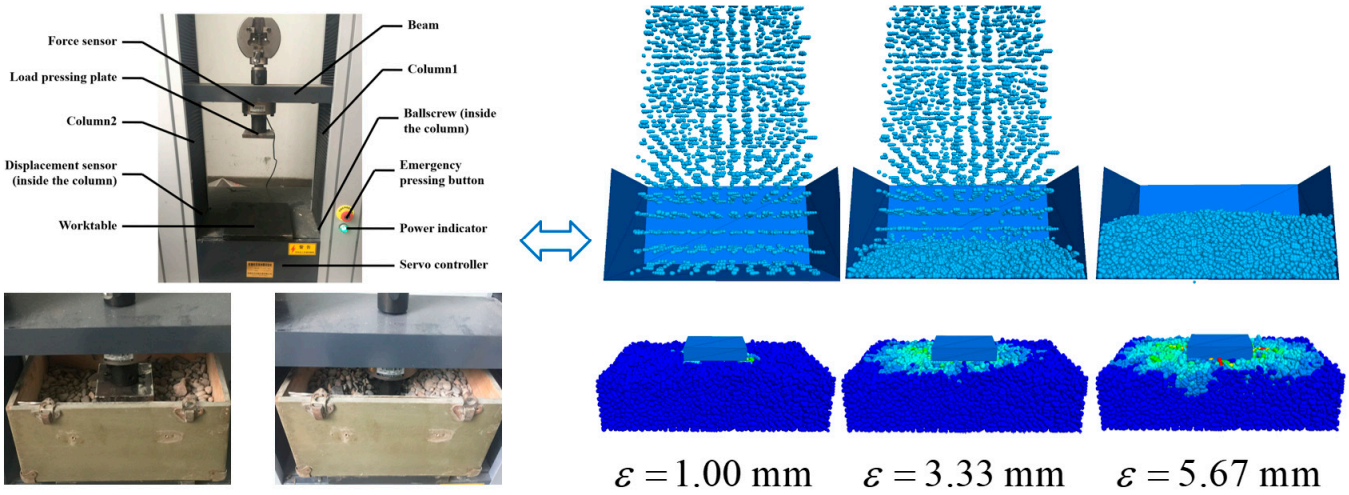


Figure 7. Testing and simulation procedures.

During the testing procedure, a container with pebbles was first placed on the worktable, with the pebble layer's thickness preset to 0.0885 m. A pressing plate then descended at a velocity of 200 mm/min, gradually compressing the pebble layer. Data on displacement and applied forces were meticulously recorded throughout this process.

After the established testing procedure, the simulation was conducted as follows: A container was first constructed and then filled with pebbles using the rainfall method. Subsequently, a pressing plate with specified dimensions was crafted and lowered into the pebble bed at the same velocity as observed in the test procedures. The contact forces acting upon the pressing plate were meticulously recorded throughout these steps. Figure 8 depicts the variations in the results attributable to the different friction parameters, and Table 1 provides the additional detailed parameters.

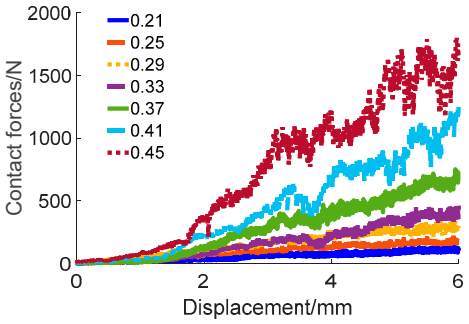


Figure 8. Simulation results with different friction parameters.

Table 1. Simulation parameters.

	Parameter	Value
Pressing plate	Length	0.1 m
	Width	0.1 m
	Height	0.01 m
Pebble container	Length	0.343 m
	Width	0.236 m
	Height	0.164 m
Pebbles	Damp	0.7 N/(m·s)
	Density	2777 kg/m^3
	Normal stiffness	4.8×10^6 N/m
	Tangential stiffness	2.4×10^7 N/m

Upon comparison with the experimental results [12], the friction parameter was determined to be 0.37. Repetitive simulations were performed to further validate the simulation outcomes. The results are depicted in Figure 9.

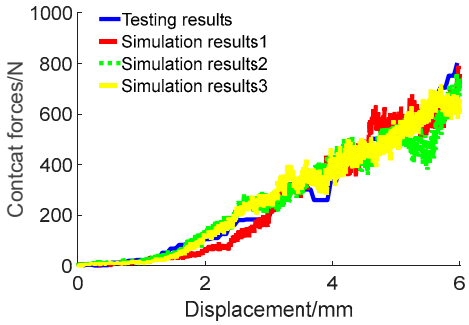


Figure 9. Repetitive simulation results.

3. Simulation Results and Analysis

3.1. Macroscopic Behaviour

The force–displacement graph is depicted in Figure 10, using a specific simulation result as an illustration.

An analysis of Figure 10 indicates that the curve can be distinctly categorised into two phases: the 'smooth period' and the 'stressed period'. The smooth period ranges from 0 mm to 1.00 mm, during which the contact force gradually escalates from 0 N to 14.87 N, exhibiting a relatively slow rate of increase. By contrast, the stressed period spans from 1.00 mm to 6.00 mm, where the contact forces markedly surge to approximately 625 N. The curve exhibits several fluctuations throughout this phase.

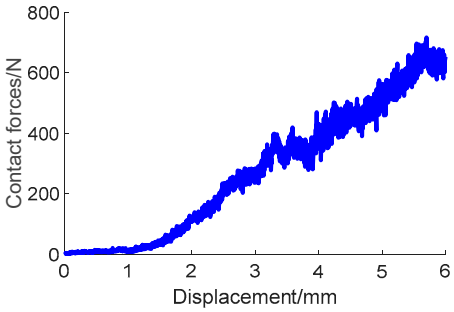


Figure 10. Simulation results.

3.2. Microscopic Behaviour

A detailed analysis of microscopic behaviour was conducted to further investigate the underlying causes behind the compression outcomes. This step included an examination of the simulation results related to pebble velocities, force chains, contact force distributions and contact force directions.

(1) Pebble velocities

The states of pebble velocities under various compressive displacement conditions are illustrated in Figure 11.

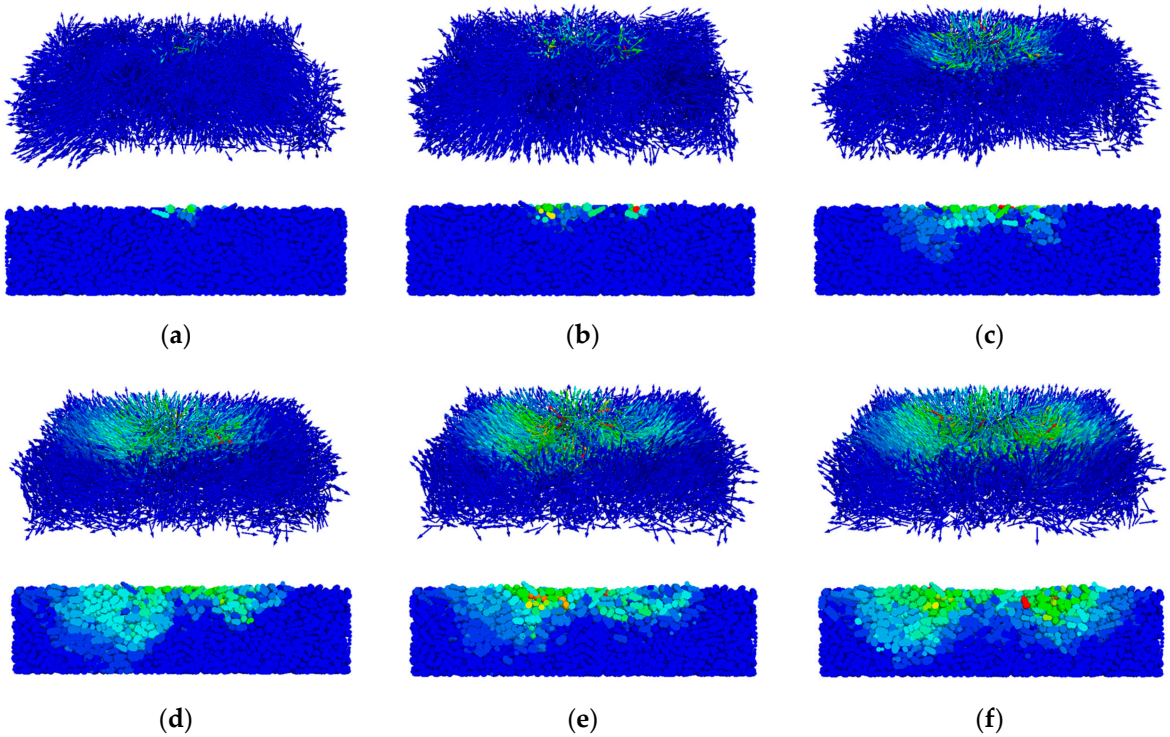


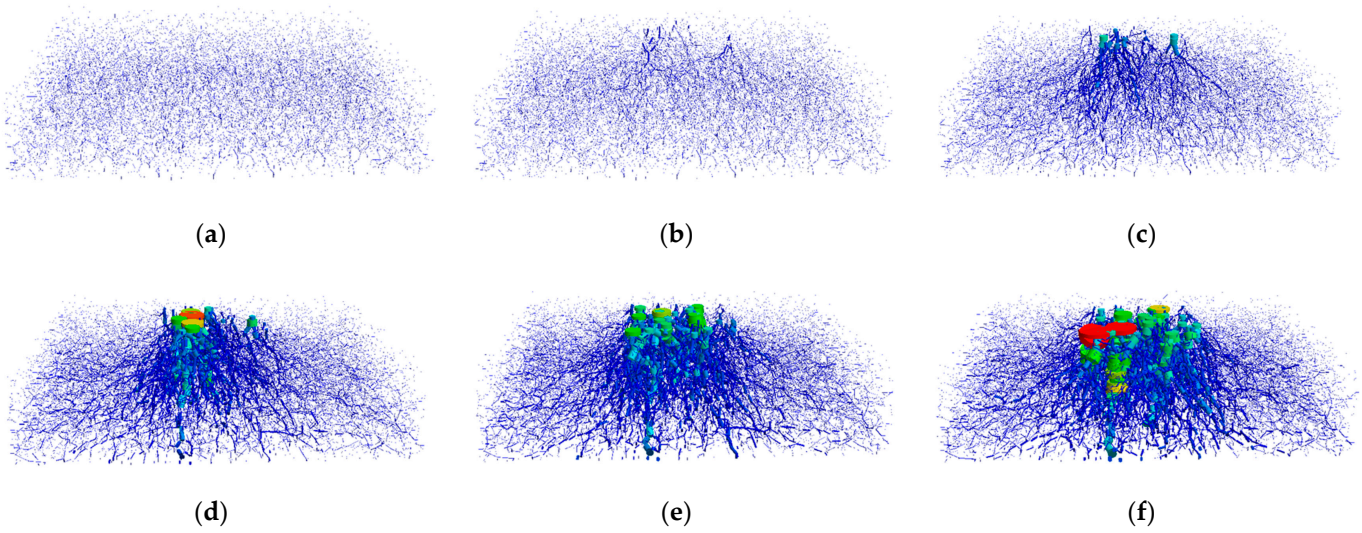
Figure 11. Pebble velocities under various compressive displacement conditions. (**a**) 0 mm; (**b**) 1 mm; (**c**) 2 mm; (**d**) 3 mm; (**e**) 4 mm; (**f**) 5 mm.

Upon the downward application of the pressing plate, the particles initiate a descending motion, with the impacted range expanding as the plate continues to press down, as can be seen from the above-mentioned figure. A cross-sectional analysis at the centre reveals that initially only a few particles in direct contact with the pressing plate are stimulated. At a depth of 0–2 mm, particles begin to compress against each other, intensifying with further penetration. In the range of 3 mm to 5 mm, acceleration is observed on the sides, whilst the centre exhibits a slower velocity. This phenomenon indicates that initially only the surface particles are affected by the pressing force. However, the force transmission amongst parti-

cles propagates as the plate penetrates deeper, causing those directly beneath the plate to descend synchronously and those around the periphery to accelerate. The central particles experience compression from the sides, resulting in less noticeable positional changes.

(2) Force chains

The states of force chains under various compressive displacement conditions are illustrated in Figure 12.



(**a**) (**b**) (**c**)

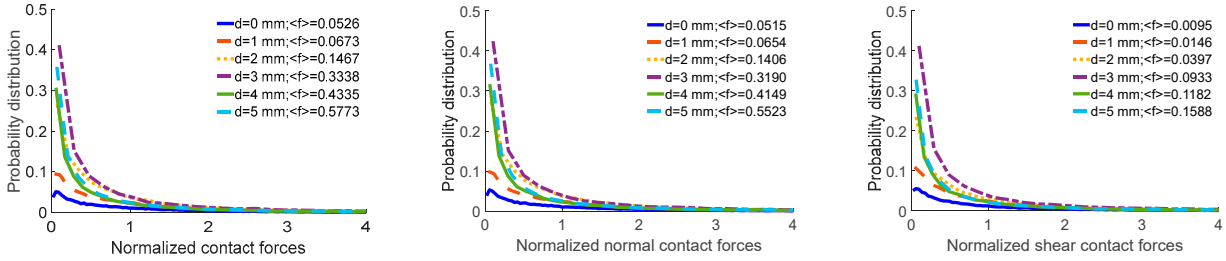
(**d**) (**e**) (**f**)

Figure 12. Force chains under various compressive displacement conditions. (**a**) 0 mm; (**b**) 1 mm; (**c**) 2 mm; (**d**) 3 mm; (**e**) 4 mm; (**f**) 5 mm.

Overall, the force chain distribution exhibits a root-like pattern, as illustrated in the above-mentioned figure. The force chain continues to expand with the progressive increase in the displacement of the pressing plate, particularly noting that the central stress predominantly concentrates in the lower part of the pressing plate's centre.

(3) Contact force distributions

During the simulation, the contact forces between all particles were quantified, with the corresponding probability density distribution illustrated in Figure 13.



(**a**) (**b**) (**c**)

Figure 13. Probability density distribution of the contact forces. (**a**) contact forces; (**b**) normal contact forces; (**c**) shear contact forces.

The average contact force between particles gradually increases with the continuous pressing of the plate, as illustrated in the above-mentioned figure. Under the same displacement, the probability distributions of the contact forces, normal contact forces and shear contact forces are essentially consistent. The force application process under varying displacements was categorised into three stages to further investigate the variations in the probability density distribution of the contact forces at different displacements. The results are depicted in Figure 14.

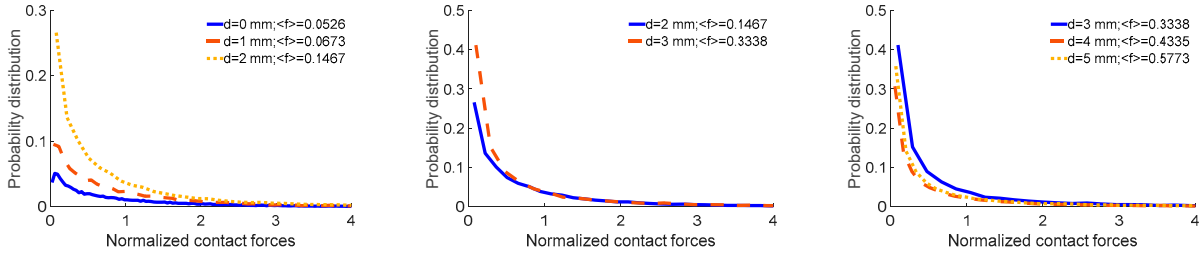


Figure 14. Probability density distribution of the contact forces at different displacements. (**a**) 0–2 mm; (**b**) 2–3 mm; (**c**) 3–5 mm.

In Stage 1 (0–2 mm), a significant intensification can be observed in the overall distribution of contact forces. This intensification is primarily due to the emergence of stronger contact forces, resulting in an elevated average contact force, whilst the majority of existing forces remain unchanged.

In Stage 2 (2–3 mm), the dynamic change in contact forces experiences a slowdown attributed to the consistent displacement leading to stress being distributed amongst a larger number of particles. This extensive stress distribution ensures that the average contact force distribution remains relatively stable as the displacement progresses.

In Stage 3 (3–5 mm), a notable shift occurs with a decrease in smaller forces, resulting in the establishment of a new equilibrium. The particles surrounding the pressing plate exhibit increased motion as compression progresses, forming a cyclic pattern. This phenomenon results in lower contact forces compared with earlier stages, with a significant reduction observed in weaker forces. Meanwhile, the distribution of larger forces becomes more distinct, showing minimal changes in subsequent transformations. This pattern is primarily due to the deceleration of internal particle movement caused by spatial constraints, resulting in a synchronous increase in the overall contact force with little change in the distribution pattern.

(4) Contact force directions

The directions of the strong contact forces (those exceeding the average value) were summarised, along with the probability distribution of these directions, based on the statistical data of particle forces. The results are shown in Figure 15.

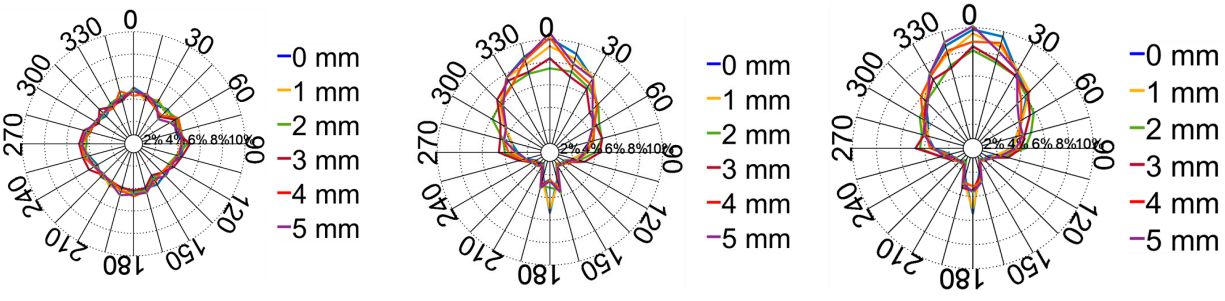
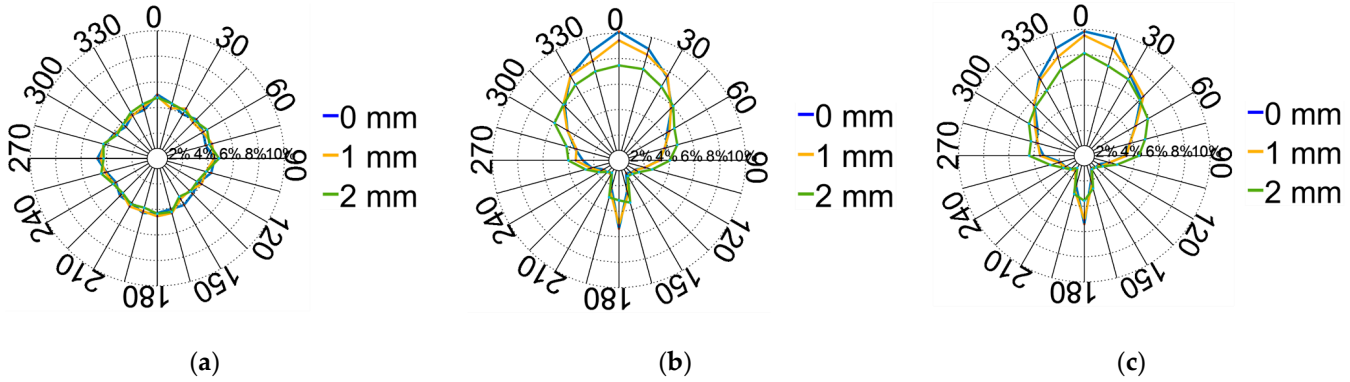


Figure 15. Probability distribution of the strong contact force directions in different planes. (**a**) XOY; (**b**) XOZ; (**c**) YOZ.

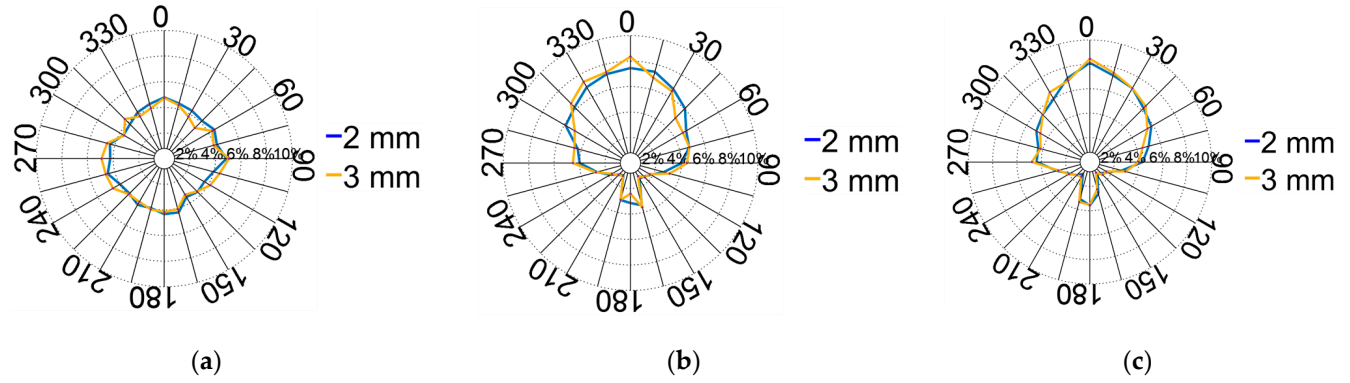
In the XOY plane, the distribution exhibits symmetry, converging towards the vertex along the three axes and forming a rectangular pattern that closely aligns with the geometry of the pressing plate. In the XOZ plane, the distribution takes on a leaf-like shape, primarily concentrated along the longitudinal axis at 0°, a characteristic consistent across the YOZ and XOZ planes. The process under varying displacements was categorised into three stages to

further investigate the variations in the probability distribution of the strong contact force directions at different displacements. The results are depicted in Figures 16–18.



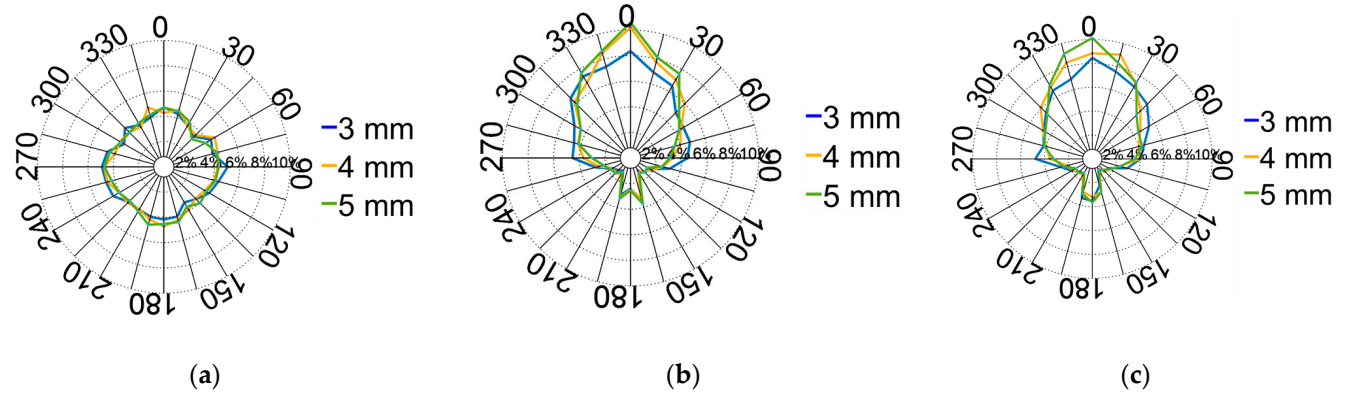
(**a**) (**b**) (**c**)

Figure 16. Probability distribution of the strong contact force directions from 0 mm to 2 mm. (**a**) XOY; (**b**) XOZ; (**c**) YOZ.



(**a**) (**b**) (**c**)

Figure 17. Probability distribution of the strong contact force directions from 2 mm to 3 mm. (**a**) XOY; (**b**) XOZ; (**c**) YOZ.



(**a**) (**b**) (**c**)

Figure 18. Probability distribution of the strong contact force directions from 3 mm to 5 mm. (**a**) XOY; (**b**) XOZ; (**c**) YOZ.

In the 0–2 mm range, the distribution variance on the XOY plane is significantly lower compared with that on the XOZ plane, with a gradual reduction in the Z-directional distribution. This observation is primarily due to the particle orientation along the Z-axis, a result of the initial particle arrangement using the rainfall method. The particles beneath the pressing plate undergo a downward compression, with the gradual increase in pressing force causing lateral dispersion and an increase in transverse forces. The distribution observed in the YOZ plane mirrors that in the XOZ plane.

In the 2–3 mm range, variations in the XOY distribution are marginal, whilst disparities in the XOZ distribution are minimal. This uniformity can be attributed to the consistent downward pressure applied by the pressing plate, which facilitates a synchronous flow amongst particles, resulting in a reduced variation in distribution. Hence, the distribution differences decrease, and the YOZ plane distribution closely mirrors that of the XOZ plane.

In the 3–5 mm range, the variation on the XOY plane remains minimal, whereas significant compression resistance on the XOZ plane disrupts the previously established equilibrium, causing an overall downward movement. This effect is markedly observed in the YOZ and XOZ planes, where a consistent pattern of downward trajectory is exhibited.

3.3. Macro–Micro Analysis

The process evolves through three stages by combining macro and micro simulation results. In the initial 0–2 mm stage, particle compression begins, intensifying with deeper penetration and affecting primarily surface particles. This stage observes a notable increase in contact force distribution due to stronger forces elevating the average contact force, whilst most existing forces remain stable. The XOY plane's variance is lesser than the XOZ's, with the Z-directional distribution gradually diminishing due to the initial Z-axis particle orientation from the rainfall method. Particles undergo compression and lateral dispersion with the increase in pressure, enhancing transverse forces, with YOZ and XOZ plane distributions mirroring each other. In the 2–3 mm stage, contact force changes slow down due to the stress distribution amongst more particles, maintaining a stable average contact force distribution. This stage's uniformity results from the pressing plate's consistent pressure, minimising distribution variations, with YOZ closely reflecting XOZ distributions. During the 3–5 mm stage, smaller forces decrease, establishing a new equilibrium and increasing particle motion around the pressing plate, forming a cyclic pattern. This phenomenon results in reduced contact forces, particularly weaker ones, whilst larger force distribution becomes more pronounced with minimal subsequent changes, primarily due to spatial constraints slowing internal particle movement, causing a synchronous overall contact force increase with stable distribution patterns.

4. Conclusions

This study employed the discrete element method to analyse arrester bed aggregates within typical truck escape ramps, aiming to identify key factors that influence their load-bearing capacity. By gathering detailed morphological characteristics of pebbles, this research introduced a novel method for generating random shapes that more accurately reflect their natural appearance. Additionally, leveraging the physical properties of the aggregates, this study developed an accurate discrete element model for the particles. This model effectively simulated the dynamic interactions between particles and investigated both macroscopic and microscopic elements that affect the aggregate's load-bearing capacity. Consequently, it revealed the dynamics of mechanical distribution among particles under external loads. These findings illuminate the factors impacting arrester bed performance and offer crucial insights into the design and utilization of pebble clusters, thereby facilitating the optimization of critical parameters for arrester beds. Within the limitations, the following conclusions can be drawn from this study:

(1) A novel approach for constructing DEM models of irregularly shaped particles is introduced, leveraging three-view outline curves to create three-dimensional DEM particle shapes via an overlapping element construction method. Comparison with actual particles reveals that this method effectively replicates the formation of pebbles, particularly those with smooth boundaries and flattened shapes. Furthermore, the method substantially decreases the quantity of basic units required to form the particles, maintaining shape fidelity while significantly reducing computational demands. The employment of open-top box compression tests to calibrate the microscopic parameters of the model indicates a consistent trend between experimental outcomes and simulation predictions, showcasing distinct variances under varied parameters

and confirming the method's viability. Moreover, the precision of the developed pebble particle DEM models is rigorously confirmed through extensive simulation and experimental verification.

(2) Leveraging the inherent material properties of these aggregates, this study provides a detailed analysis of the mechanical behavior of aggregate particles. At the macroscopic level, it conducts an analytical exploration of the stress–strain relationship curve, which is divided into two distinct phases: the 'smooth phase' and the 'stress phase.' The smooth phase signifies a relatively moderate growth rate, whereas in the stress phase, the contact force sharply increases, marked by several fluctuations throughout. On the microscopic scale, this study outlines the transmission pathways of external loads and the mechanical interactions between individual particle units, highlighting the particle as the primary unit of analysis. It shows that external pressures mainly affect surface-level particles initially. As the application of pressure intensifies, the distribution of force among particles becomes wider, causing a synchronous downward movement of particles under direct pressure, while adjacent ones undergo accelerated displacement. Centrally located particles experience lateral compression, leading to more subtle positional changes.

(3) Integrating macroscopic and microscopic contact characteristics, this analysis delineates the process into three phases. Initially, there's a marked increase in contact forces, boosting the average force while maintaining stability. Notably, the XOY plane shows less variability than the XOZ plane, with YOZ and XOZ distributions essentially consistent, which is attributed to the particles' initial Z-axis orientation via the rainfall method. Subsequently, the rate of change in contact force decelerates due to the dispersed stress distribution, ensuring consistent average force. This uniformity stems from the pressing plate's even pressure, aligning YOZ with XOZ distributions. The concluding phase features reduced minor forces, fostering a new equilibrium and heightened particle mobility, thus forming a cyclic pattern. Minimal subsequent changes, largely due to spatial constraints, lead to an increased contact force and stable distribution.

This study represents a significant advancement in understanding the load-bearing capacity of pebble aggregates, yet it also highlights existing unresolved questions and limitations. The construction of the DEM model relies on specific physical and morphological parameters of pebbles, potentially limiting its broad application and adaptability to various pebble materials. Moreover, while the DEM provides detailed simulations of particle interactions, its demands for computational resources and time may restrict its use for large-scale or real-time analysis.

Considering the insights and constraints identified in this study, future research should focus on key areas, including utilizing high-resolution 3D scanning technology to create high-precision models that incorporate a wide array of morphological features, enhancing the model's universality and predictive accuracy. Efforts should also aim to expand the discrete element model's utility to accurately represent a diverse array of pebble types, mirroring real-world gravel particle shapes, and to analyze the load-bearing capacity of aggregates with various shape characteristics. Furthermore, improving the computational efficiency of the DEM model is essential for facilitating large-scale and real-time analysis of arrester bed performance.

Author Contributions: Conceptualization, P.L.; methodology, P.B.; software, W.L.; validation, P.L., P.B. and W.L.; formal analysis, P.L.; investigation, P.B.; resources, P.L.; data curation, W.L.; writing—original draft preparation, P.L.; writing—review and editing, P.B.; visualization, P.L.; supervision, W.L.; funding acquisition, P.L. All authors have read and agreed to the published version of the manuscript.

Funding: This research was supported by the Natural Science Foundation of Henan (Grant NO. 242300421446) and the Key Research and Development and Promotion Project of Henan Province (Grant NO. 212102310483).

Institutional Review Board Statement: Not applicable.

Informed Consent Statement: Not applicable.

Data Availability Statement: Data are contained within the article.

Conflicts of Interest: The authors declare no conflicts of interest.

References

1. Haq, M.T.; Ampadu, V.M.K.; Ksaibati, K. An investigation of brake failure related crashes and injury severity on mountainous roadways in Wyoming. *J. Saf. Res.* **2023**, *84*, 7–17. [CrossRef] [PubMed]
2. He, Y.; Wang, Y.; Wu, F.; Yang, R.; Wang, P.; She, S.; Ren, D. Temperature monitoring of vehicle brake drum based on dual light fusion and deep learning. *Infrared Phys. Technol.* **2023**, *133*, 104823. [CrossRef]
3. Qin, P.; Li, Z.; Li, H.; Huang, J.; Wang, G. Influence of Aggregate Pollution in Truck Escape Ramps on Stopping Distance of Uncontrolled Vehicles. *Sustainability* **2022**, *14*, 11593. [CrossRef]
4. Capuano, F.A.; Heymsfield, E.; Li, N. Alternative arresting system design for truck escape ramps. *Int. J. Crashworthiness* **2018**, *23*, 618–626. [CrossRef]
5. van der Haven, D.L.H.; Fragkopoulos, I.S.; Elliott, J.A. A physically consistent Discrete Element Method for arbitrary shapes using Volume-interacting Level Sets. *Comput. Methods Appl. Mech. Eng.* **2023**, *414*, 116165. [CrossRef]
6. Cundall, P.A.; Strack, O.D.L. A discrete numerical model for granular assemblies. *Geotechnique* **1979**, *29*, 47–65. [CrossRef]
7. Ren, J.; Yin, C. Investigating mechanical characteristics of aggregate structure for road materials. *Int. J. Pavement Eng.* **2022**, *23*, 372–386. [CrossRef]
8. Zhao, X.; Dong, Q.; Chen, X.; Xiao, Y.; Zheng, D. Fatigue damage numerical simulation of cement-treated base materials by discrete element method. *Constr. Build. Mater.* **2021**, *276*, 122142. [CrossRef]
9. Li, J.; Wang, B.; Wang, D.; Zhang, P.; Vardon, P. A coupled MPM-DEM method for modelling soil-rock mixtures. *Comput. Geotech.* **2023**, *160*, 105508. [CrossRef]
10. Haq, S.; Indraratna, B.; Nguyen, T.T.; Rujikiatkamjorn, C. Hydromechanical state of soil fluidisation: A microscale perspective. *Acta Geotech.* **2023**, *18*, 1149–1167. [CrossRef]
11. Lin, J.; Bao, M.; Zhang, F.; Yang, J.; Li, H. Mixing simulation of cohesive particles in a soil mixer. *Powder Technol.* **2022**, *399*, 117218. [CrossRef]
12. Liu, P.; Yu, Q.; Zhao, X.; Zhou, C.; Shi, P. Three-dimensional discrete element modeling of the irregularly shaped pebbles used in a truck escape ramp. *Comput. Part. Mech.* **2020**, *7*, 479–490. [CrossRef]
13. Zhao, X.; Liu, P.; Yu, Q.; Shi, P.; Ye, Y. On the effective speed control characteristics of a truck escape ramp based on the discrete element method. *IEEE Access* **2019**, *7*, 80366–80379. [CrossRef]
14. Sun, W.; Wu, K.; Liu, S.; Zhang, X. Influence of aspect ratio and arrangement direction on the shear behavior of ellipsoids. *Particuology* **2022**, *70*, 82–94. [CrossRef]
15. Golshan, S.; Munch, P.; Gassmöller, R.; Kronbichler, M.; Blais, B. Lethe-DEM: An open-source parallel discrete element solver with load balancing. *Comput. Part. Mech.* **2023**, *10*, 77–96. [CrossRef]
16. Han, J.; Shen, K.; Guo, Y.; Xiong, H.; Lin, J. Discrete element simulations of flexible ribbon-like particles. *Powder Technol.* **2023**, *429*, 118950. [CrossRef]
17. Yang, P.; Kavazanjian, E.; Neithalath, N. DEM simulations on the influence of carbonate precipitation on liquefaction mitigation of sand. *Comput. Geotech.* **2023**, *162*, 105681. [CrossRef]
18. Li, X.; Kouretzis, G.; Thoeni, K. Discrete Element Modelling of uplift of rigid pipes deeply buried in dense sand. *Comput. Geotech.* **2024**, *166*, 105957. [CrossRef]
19. Pawar, D.K.; Annabattula, R.K.; Swaminathan, N. Mesoscopic mechanics of triaxially compressed pebble assembly and estimation of Drucker–Prager parameters using discrete element method. *Comput. Part. Mech.* **2023**, 1–17. [CrossRef]
20. Coetzee, C. Calibration of the discrete element method: Strategies for spherical and non-spherical particles. *Powder Technol.* **2020**, *364*, 851–878. [CrossRef]
21. Liu, X.; Zhou, A.; Sun, K.; Shen, S.-L. Discrete element modelling of the macro/micro-mechanical behaviour of unsaturated soil in direct shear tests including wetting process. *Powder Technol.* **2023**, *415*, 118125. [CrossRef]
22. Lai, Z.; Xia, Y.; Chen, Q. Discrete element modeling of granular hopper flow of irregular-shaped deformable particles. *Advanced Powder Technol.* **2023**, *34*, 104106. [CrossRef]
23. Huang, X.; Zheng, Q.; Liu, D.; Yu, A.; Yan, W. A design method of hopper shape optimization with improved mass flow pattern and reduced particle segregation. *Chem. Eng. Sci.* **2022**, *253*, 117579. [CrossRef]

24. Canny, J. A computational approach to edge detection. *IEEE Trans. Pattern Anal. Mach. Intell.* **1986**, *6*, 679–698. [CrossRef]
25. Liu, P.; Yu, Q.; Zhao, X.; Shi, P.; Chen, H. Discrete element analysis of the reconstruction method for randomly shaped pebbles. *IEEE Access* **2019**, *7*, 137317–137329. [CrossRef]

Disclaimer/Publisher's Note: The statements, opinions and data contained in all publications are solely those of the individual author(s) and contributor(s) and not of MDPI and/or the editor(s). MDPI and/or the editor(s) disclaim responsibility for any injury to people or property resulting from any ideas, methods, instructions or products referred to in the content.